Investigation of the nacelle blockage effect for a downwind turbine

Benjamin Anderson[1], **Emmanuel Branlard**[1], **Ganesh Vijayakumar**[1], **Nick Johnson**[1]

[1]National Renewable Energy Laboratory, Golden, CO, USA.

E-mail: benjamin.anderson@nrel.gov

Abstract. As downwind turbines garner increasing research interest, nacelle blockage becomes an important consideration. This paper examines nacelle blockage effects under a variety of Reynolds numbers, turbulence intensities, and nacelle geometries and proposes a computationally inexpensive nacelle blockage engineering model. Results show minimal nacelle blockage impacts on rotor loading and performance, except for tall (low-aspect-ratio) nacelles, which can cause an increase in rotor C_p of up to 0.6%. In all cases, nacelle blockage increases rotor loading and performance metrics, however little. Finally, (more expensive) geometry-resolved and (less expensive) body-force computational fluid dynamics modeling techniques are compared, and body-force models are found to need improvement to adequately model nacelle blockage.

1. Introduction

As wind turbines increase in size and blades continue to grow longer, downwind turbines are garnering increased research interest because of the relaxed stiffness constraint on the blades. Downwind turbines offer a number of advantages and challenges relative to upwind turbines, and tools to model downwind-specific physics are crucial to moving this technology forward. Key modeling needs include nacelle blockage and tower shadow aeroelastic effects. Most aeroelastic tools, such as the open-source code OpenFAST [1], include tower wake effects but neglect nacelle effects. The development of reliable, cost-effective downwind turbines requires robust modeling tools that can examine the effects of nacelle blockage and wake on the rotor. This article demonstrates the effect of nacelle blockage and proposes an engineering model (EM) that could be adopted into aeroelastic codes to enable this analysis. The model may also be used for upwind turbines. The term nacelle is used to denote the entire nacelle and hub assembly because it is the combined aerodynamic effect of both bodies that is usually understood as the nacelle blockage effect.

Ameur et al. [2] found nacelle impacts on inflow wind speed to be insignificant for upwind machines, but downwind nacelle impacts may significantly affect rotor loading and performance caused by nacelle blockage. Wang et al. [3] compared upwind and downwind turbines experimentally and found that nacelle and tower-induced vortices cause high turbulent kinetic energy and that low momentum flow exists right behind the nacelle. They further noticed that downwind turbines shed larger vortices at 60%–70% along the blade span and postulated that this may be caused by nacelle and tower blockage. Frau et al. [4] found that downwind turbines

have higher power, thrust, root bending, and unsteady loading than upwind. The trend was explained by the nacelle redirecting inflow outward along the blade span to more aerodynamically efficient blade sections. However, it is unclear whether higher loading is caused by tower wake alone or tower and nacelle wake combined. Bortolotti et al. [5] ran a design comparison between upwind and downwind turbines, noting that downwind turbines generate lower annual energy production and in turn yield higher cost of energy, but that results could change if nacelle blockage had a beneficial effect on power production. Santoni et al. [6] found that the nacelle and tower wake contribute significantly to wind turbine wake for upwind machines, both by increasing the velocity deficit downstream of the turbine and by interacting with the rotor wake to increase the mean kinetic energy flux into the wake. They further determined that including tower and nacelle blockage in their model yielded results closer to those from experiment. In another study, Kress et al. [7] found that, because of nacelle blockage accelerating flow into the rotor, downwind turbine performance is less sensitive to variations in flow inclination.

In light of the presence of a nacelle wake, and indications that nacelle blockage could have significant effects on both rotor loads and aerodynamic power, blockage effects from a wind turbine nacelle are examined for a downwind concept machine, known as the Big Adaptive Rotor (BAR) turbine, which was designed for onshore applications. The research questions considered in this paper are:

1. Does nacelle blockage have significant effects on rotor loading and performance?
2. Can a low-computational-cost engineering model (EM) be developed to accurately capture nacelle blockage effects on the flow field?
3. Do less computationally expensive body-force computational fluid dynamics (CFD) models capture the nacelle blockage effects as well as geometry-resolved CFD models?

To answer the first research question, the acceleration of the flow around the nacelle is predicted using geometry-resolved CFD simulations of different nacelle shapes. Then, using a blade element momentum (BEM) code, rotor loading and aerodynamic power are compared with and without the presence of nacelle blockage. To answer the second question, an EM is created and validated using geometry-resolved CFD simulations. To answer the final question, the flow field and resulting rotor loading/performance are compared for body-force and geometry-resolved nacelle blockage models.

2. Methods

In Section 2.1, several suites are defined, consisting of CFD runs, that will be used to determine the effects of nacelle blockage on rotor loads and performance and to assess the efficacy of the body-force CFD methods and the EM. In Section 2.2, a computationally inexpensive EM is presented that approximates the flow about the nacelle using the analytical velocity field about an ellipsoid of revolution. In Section 2.3, an in-house BEM code is described that will calculate rotor loads and performance based on the flow field results from the CFD and EM.

CFD and EM results are time averaged, thus smearing the dynamic effects of turbulence and vortex shedding. The effects of the rotor on the nacelle flow are assumed to be weak and so are neglected. A rigid rotor is used because this work focuses on aerodynamic aspects and does not consider the fatigue effects of dynamic loading.

The nacelles and EM representations considered for the CFD and EM are displayed in Figure 1. Four ellipsoid nacelles are considered, with aspect ratios (length/height) of 4, 2, 1, and 2/3. A pill, rectangle, and bullet geometry are also considered. All nacelles are 20-m long.

2.1. CFD simulation setup

Several suites of CFD runs are performed, as detailed in Table 1. The suites consider various

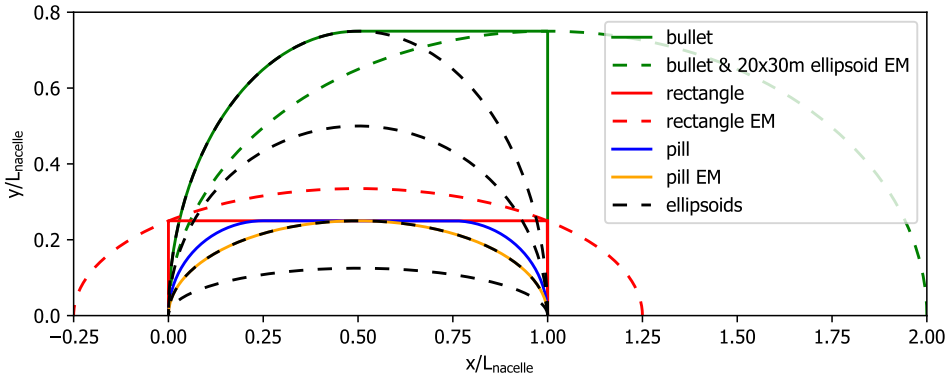

Figure 1. The nacelles and EM representations considered. The rectangle, pill, and bullet are approximated by ellipsoids in the EM.

Table 1. Suite descriptions.

Suite	Objective	Parameters Varied
1	Determine if root airfoils respond to nacelle blockage effects	Root airfoils
2	Determine blockage effects of different nacelle geometries	Nacelle shape (ellipsoid, pill, and rectangle)
3	Determine blockage effects of different nacelle aspect ratios	Nacelle height [5, 10, 20, 30] m
4	Determine relationship between Re and blockage effects	Inflow velocity [3, 15, 25] m/s
5	Compare CFD models; determine blockage effect of TI	CFD method (body-force/geometry-resolved), TI

nacelle shapes, inflow turbulence intensities (TI), and Reynolds numbers (Re). The commercial CFD solver Fluent is used for all except the last suite, where body-force and geometry-resolved models are compared using the research CFD code ExaWind [8].

2.1.1. Suites 1–4 CFD solver: Fluent. The ANSYS Fluent solver is used to perform the steady-state Reynolds-averaged Navier-Stokes (RANS) simulations for suites 1–4 using the k-ω shear stress transport (SST) turbulence model. The CFD simulations are performed on a rectangular prism fluid domain around a quarter of the 20-m-long nacelle. Relative to the nacelle center, the domain extends 150 m above, 150 m laterally, 200 m in front, and 300 m behind. The mesh is refined along the nacelle surface with a resolution of 0.2 m. A hyperbolic extrusion is used to grow the surface mesh on the nacelle to 60 layers with a first cell height of 5×10^{-5}m (corresponding to $y^+ = 1$) and a growth ratio of 1.2. Tetrahedral elements and pyramidal elements fill the rest of the domain, as shown in Figure 2. An example of flow field for an ellipsoid nacelle is displayed on the left of Figure 3.

2.1.2. Suite 5 CFD solver: ExaWind. The incompressible CFD solver Nalu-wind in the ExaWind framework [8] is used to compare the body-force and geometry-resolved CFD modeling approaches at different TIs. The ExaWind framework is used instead of ANSYS Fluent because it provides both body-force and geometry-resolved CFD modeling

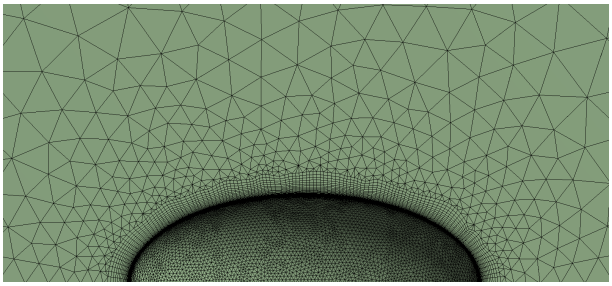

Figure 2. Fluent fluid mesh zoomed in on the 20 x 10-m ellipsoid nacelle. A quarter of the flow field is modeled.

capabilities along with turbulence injection at a specified intensity. The actuator-force approach [9] approximates the effect of the nacelle on the flow field using a body-force term at the nacelle location in the momentum equation. The body-force $\vec{F}$ applied by the nacelle on the flow field is calculated to be in the direction of the velocity sampled at the nacelle location in the CFD domain using a specified drag coefficient C_D and velocity sampled at the location of the nacelle $\vec{V}_{\text{sample}}$ as

$$\vec{F} = \frac{1}{2}\rho V_{cor}\vec{V}_{\text{sample}}C_D A, \tag{1}$$

where ρ is the density, A is the frontal area, and V_{cor} is the velocity corrected to account for the Gaussian spreading of the actuator force, as shown by Martinez et al. [10]. While geometry-resolved CFD simulations can capture the complex flow around arbitrary shapes, the body-force approach is computationally far cheaper (approximately 45 times cheaper in this case).

The geometry-resolved CFD simulations are first performed using the unsteady RANS approach with the k-ω-SST turbulence model at three different TIs for the same inflow velocity. Then the actuator-force CFD simulations are performed using the average drag coefficient extracted from the geometry-resolved CFD simulations and the same inflow conditions. The inflow turbulence is generated using the Mann model [11], and the turbulence is injected into the flow field at a plane 30 m in front of the nacelle using the algorithm by Troldborg et al. [12]. The velocity profiles from the body-force and geometry-resolved simulations are compared. They are averaged over at least $90D/V_\infty$, where D is the length of the nacelle and V_∞ is the average freestream velocity.

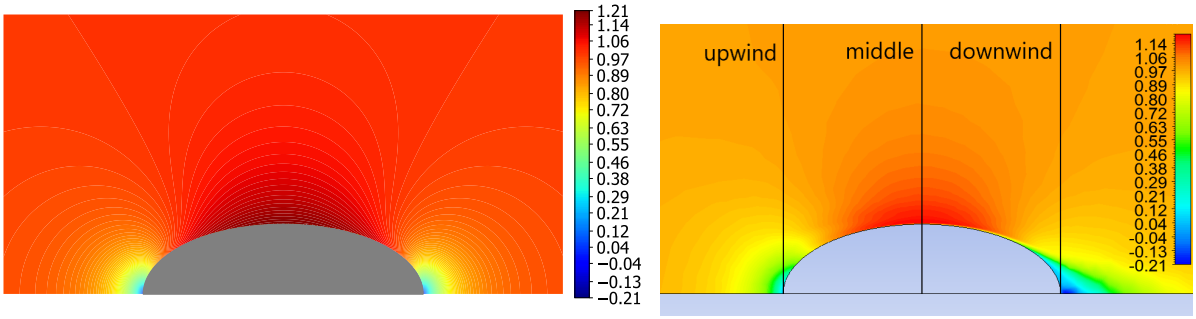

Figure 3. Normalized velocity around the 20 x 10-m ellipsoid nacelle, calculated by the EM (left) and Fluent (right). Vertical lines mark upwind, middle, and downwind planes for velocity extraction. The EM captures potential flow but not wake.

2.2. Engineering model

The EM is based on the potential velocity field about an ellipsoid of revolution. An example of the flow field is displayed on the right side of Figure 3. The derivation steps to obtain the velocity in polar coordinates are given below. An ellipsoid of revolution of semi-axes a (along x) and b (along y, z, or r) is considered. The eccentricity, e, and the distance from the origin to the foci, k, are defined respectively as: $e = \sqrt{a^2 - b^2}/a$ and $k = ea$. Lamb [13] provides the velocity potential for an ellipsoid of revolution, in terms of semi-elliptic coordinates (μ, ζ) :

$$\phi = A\mu\left[\frac{1}{2}\zeta\log\frac{\zeta+1}{\zeta-1} - 1\right], \quad \text{with} \quad A = U_0\, a\left[\frac{1}{1-e^2} - \frac{1}{2e}\log\frac{1+e}{1-e}\right]^{-1} \tag{2}$$

where U_0 is the freestream velocity, and the semi-elliptic coordinates (μ, ζ) are related to the polar coordinates (x, r) as $x = k\mu\zeta$ and $r = \sqrt{1-\mu^2}\sqrt{\zeta^2-1}$ with μ in the range $[-1, 1]$ and ζ

in the range [1, $+\infty$]. We inverted the change of variables as follows:

$$\mu = \frac{x}{k\zeta}, \quad \zeta = \frac{\sqrt{-B+\sqrt{\Delta}}}{\sqrt{2}k}, \quad \text{with} \quad B = -(k^2+x^2+r^2), \quad \Delta = B^2 - 4k^2x^2 \tag{3}$$

We obtained the velocity field in polar coordinates by taking the gradient of the velocity potential and performing the change of variable from polar to semi-elliptic coordinates:

$$u_x = \frac{\partial\phi}{\partial x} = \frac{\partial\phi}{\partial\mu}\frac{\partial\mu}{\partial x} + \frac{\partial\phi}{\partial\zeta}\frac{\partial\zeta}{\partial x} \qquad u_r = \frac{\partial\phi}{\partial r} = \frac{\partial\phi}{\partial\mu}\frac{\partial\mu}{\partial r} + \frac{\partial\phi}{\partial\zeta}\frac{\partial\zeta}{\partial r} \tag{4}$$

with

$$\frac{\partial\phi}{\partial\mu} = \frac{\phi}{\mu} \qquad \frac{\partial\mu}{\partial x} = -\frac{x}{k\zeta^2}\frac{\partial\zeta}{\partial x} + \frac{1}{k\zeta} \qquad \frac{\partial\mu}{\partial r} = -\frac{x}{k\zeta^2}\frac{\partial\zeta}{\partial r}$$

$$\frac{\partial\phi}{\partial\zeta} = \mu\frac{A}{2}\left[\log\frac{\zeta+1}{\zeta-1} - \frac{2\zeta}{\zeta^2-1}\right] \qquad \frac{\partial\zeta}{\partial x} = \frac{x}{\sqrt{\Delta}}\left[\zeta - \frac{1}{\zeta}\right] \qquad \frac{\partial\zeta}{\partial r} = \frac{r\zeta}{\sqrt{\Delta}}$$

Equation 4 is used to compute the velocity field about an ellipsoid, where the semi-axes' lengths and the center of the ellipsoid are tuned to match the flow of a given nacelle geometry and freestream velocity.

2.3. BEM model

A BEM model is developed to calculate an axial induction factor, loads, and performance along the rotor. The model follows the implementation presented in [14], with Glauert's tip-loss and high-thrust corrections. The velocity field may vary across the blade span, which allows for the nacelle blockage effect. OpenFAST input files are read in to determine rotor parameters, including rotor pitch, chord, and twist along the blade span. Based on an input velocity field and turbine design, the code determines rotor load and performance data, including: the power and thrust coefficients C_p & C_T, edgewise bending moment at blade root, and flapwise bending moment at blade root. The results from the BEM code are used to evaluate the impact of different nacelle designs on the rotor performance.

3. Results

For each run, the normalized velocity profiles and resulting changes in rotor loads are calculated. The results are reported at three "potential rotor planes" along the nacelle. The planes are located at the front, middle, and back of the nacelle (upwind, middle, downwind; see Figure 3). The inflow used for the simulations is a temporally and spatially constant 8 m/s, unless specified otherwise. The inflow with blockage is fed into the BEM model. Across all runs, nacelle blockage effects are most significant downwind, and these results will be the focus of the section. However, these models can be used for upwind or downwind.

3.1. Suite 1: Influence of root airfoils

As is typical with utility-scale turbines, the BAR utilizes a cylindrical blade section at the root that merges into an aerodynamically optimized blade profile. The suite 3 flow results (for ellipsoids with aspect ratios of 2/3 to 4) are reused as inflow into a modified rotor that uses the airfoil at a 10-m radius (a flat back airfoil) for all blade sections up to that radius. The goal is to determine if nacelle blockage would have a more significant effect on a rotor with lift-producing airfoils in the boundary layer and speedup zone. The results (not shown) reveal that the changes in root-airfoil-rotor loads and performance are similar (within 10%) to those of the original rotor. A rotor optimized for nacelle blockage was not examined, and could exhibit more significant changes in performance.

3.2. Suite 2: Influence of nacelle shape

Nacelle blockage effects are examined for a variety of nacelle shapes. An ellipsoid, rectangular prism, and pill-shaped nacelle are considered (see Figure 1). The pill-shaped nacelle consists of two hemispheres connected by a cylinder. All three nacelles are 20-m long, 10-m high, and 10-m wide. For the EM, a 20 x 10-m nacelle is used for the ellipsoid and pill cases, and an ellipsoid that intersects the rectangular prism's vertices is used for the rectangular case. The velocity profiles are shown in Figure 4 for the three planes considered. As expected, the ellipsoid-based EM matches an ellipsoid nacelle better than other geometries. The EM captures the velocity field for the first two planes well but cannot capture the separation occurring downstream. Table 2

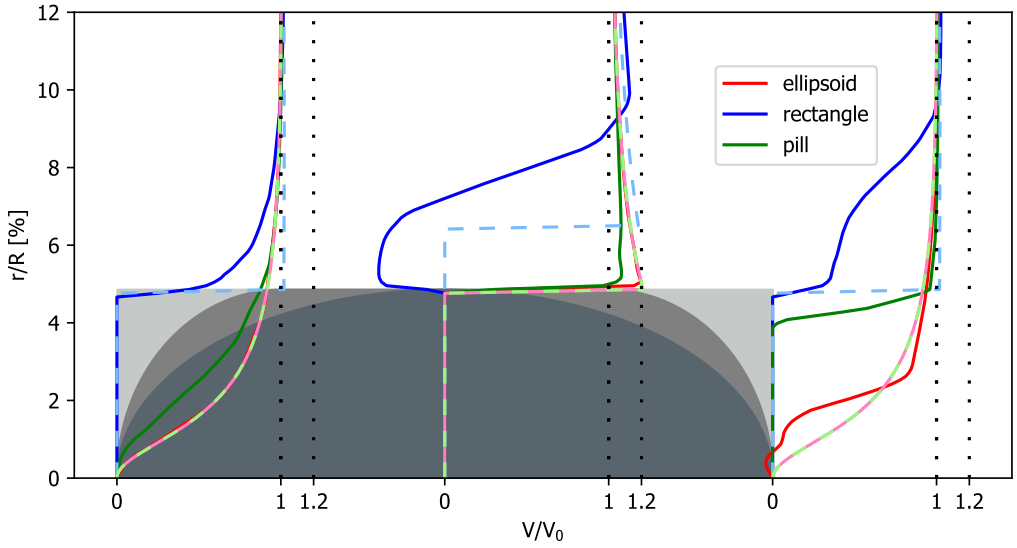

Figure 4. Normalized velocity profiles along rotor planes for various nacelle shapes. Solid, darker lines: CFD results. Dashed, lighter lines: EM results. The three rotor planes considered, from left to right, are: upwind, middle, and downwind. Note: the rectangle EM is wider in the middle.

details the results for the downwind plane. The average speedup/slowdown magnitude along the whole rotor span is found by:

$$\overline{|\,\Delta V\,|}_{\mathrm{CFD}} = \frac{1}{N}\sum_{i=1}^{i=N} |\,V(i) - V_0\,|_{\mathrm{CFD}} \tag{5}$$

where V_0 is the freestream velocity, $V(i)$ is the flow velocity at section i, and N is the number of rotor sections. Also tabulated are the resulting changes in C_p, C_T, edgewise bending moment at blade root, and flapwise bending moment at blade root. Lastly, the table shows the difference in average speedup/slowdown and C_p between CFD and EM, normalized by the CFD values:

$$E_{\Delta V} = \frac{\overline{|\,\Delta V\,|}_{\mathrm{EM}} - \overline{|\,\Delta V\,|}_{\mathrm{CFD}}}{\overline{|\,\Delta V\,|}_{\mathrm{CFD}}} \tag{6}$$

This reveals how closely they model nacelle blockage. The results from Table 2 indicate that the more bluff the body, the greater the increase in rotor loads and performance. Still, performance effects are small at $\leq$0.11%.

Table 2. Flow/BEM results for different nacelle geometries (Suite 2) at the downwind plane. Results are compared to a constant inflow case (i.e., without nacelle). Positive values in rotor outputs indicate an increased value when the nacelle is present.

Geometry	$\overline{\lvert \Delta V \rvert}_{\mathrm{CFD}}$	ΔCP_{CFD}	ΔCT_{CFD}	$\Delta Edge_{\mathrm{CFD}}$	$\Delta Flap_{\mathrm{CFD}}$	$E_{\Delta V}$	$E_{\Delta CP}$
Rectangle	7.19%	0.11%	0.04%	0.06%	0.03%	-68.51%	-80.78%
Pill	4.60%	0.03%	0.01%	0.01%	0.01%	13.83%	101.59%
Ellipsoid	2.55%	0.02%	0.01%	0.01%	0.01%	-11.18%	-18.03%

3.3. Suite 3: Influence of nacelle height

Nacelle blockage effects are examined for a variety of nacelle heights. The ellipsoid nacelles range in height from 5 m to 30 m, corresponding to aspect ratios ranging from 4 to 2/3. A bullet-shaped nacelle with aspect ratio 2/3 is also examined to determine if blockage effects can be amplified by a geometry that forces more flow outward in the downwind section. The EM is currently only applicable for ellipsoids with aspect ratios >1. To model the 20 x 30-m ellipsoid, an oversized EM ellipsoid of the same height and twice the length is used, with the downwind rotor plane located at the middle of this EM ellipsoid. This also captures the boundary layer effects, which effectively increase the thickness of the body and induce a speedup outside of the boundary layer. The 20 x 20-m CFD ellipsoid is compared to both a 20 x 20-m EM and an oversized 40 x 30-m EM. This "oversize-ellipsoid" method is also used to model the bullet nacelle. The different geometries modelled are shown in Figure 1. The bullet corresponds to the leading half of the EM ellipsoid, which has an aspect ratio of 4/3. Note that the bullet and 20 x 30-m ellipsoid EM are the same.

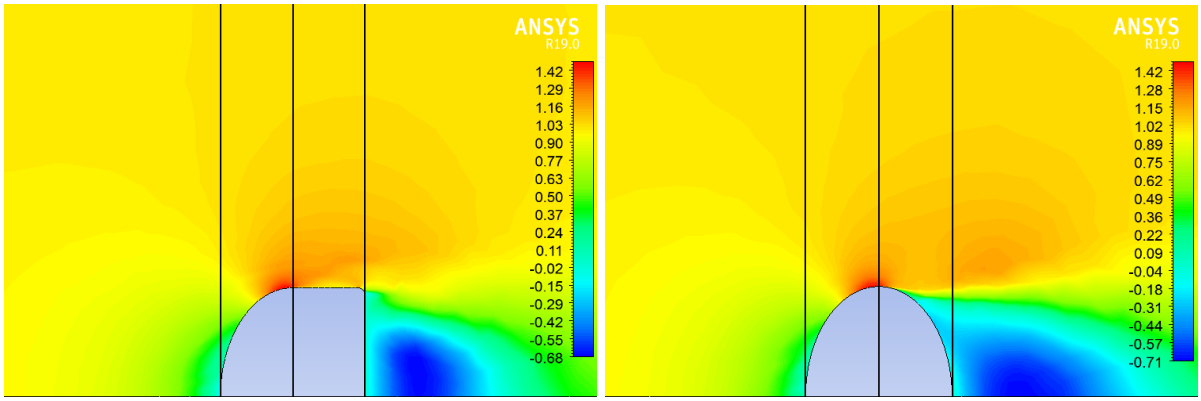

Figure 5. Normalized velocity around the 20 x 30-m bullet (left) and ellipsoid (right) nacelles, calculated by Fluent. Vertical lines mark upwind, middle, and downwind planes for velocity extraction. These nacelles show a downwind C_p increase of 0.54% and 0.61%, respectively.

Table 3. Flow/BEM results for suite 3. E=ellipsoid, B=bullet. Rotor performance and loads increase with nacelle size. Results have the best CFD-EM agreement for the bullet, followed by thin (high-aspect-ratio) ellipsoid nacelles.

Geometry	$\overline{\lvert \Delta V \rvert}_{\mathrm{CFD}}$	ΔCP_{CFD}	ΔCT_{CFD}	$\Delta Edge_{\mathrm{CFD}}$	$\Delta Flap_{\mathrm{CFD}}$	$E_{\Delta V}$	$E_{\Delta CP}$
E20x5m	1.12%	0.01%	0.00%	0.00%	0.00%	-21.44%	-12.73%
E20x10m	2.55%	0.02%	0.01%	0.01%	0.01%	-11.18%	-18.03%
E20x20m original	7.39%	0.15%	0.06%	0.08%	0.04%	-23.12%	-35.16%
E20x20m oversize	7.39%	0.15%	0.06%	0.08%	0.04%	54.89%	61.17%
E20x30m	17.52%	0.61%	0.26%	0.37%	0.17%	0.57%	-0.84%
B20x30m	16.84%	0.54%	0.24%	0.33%	0.15%	4.64%	10.74%

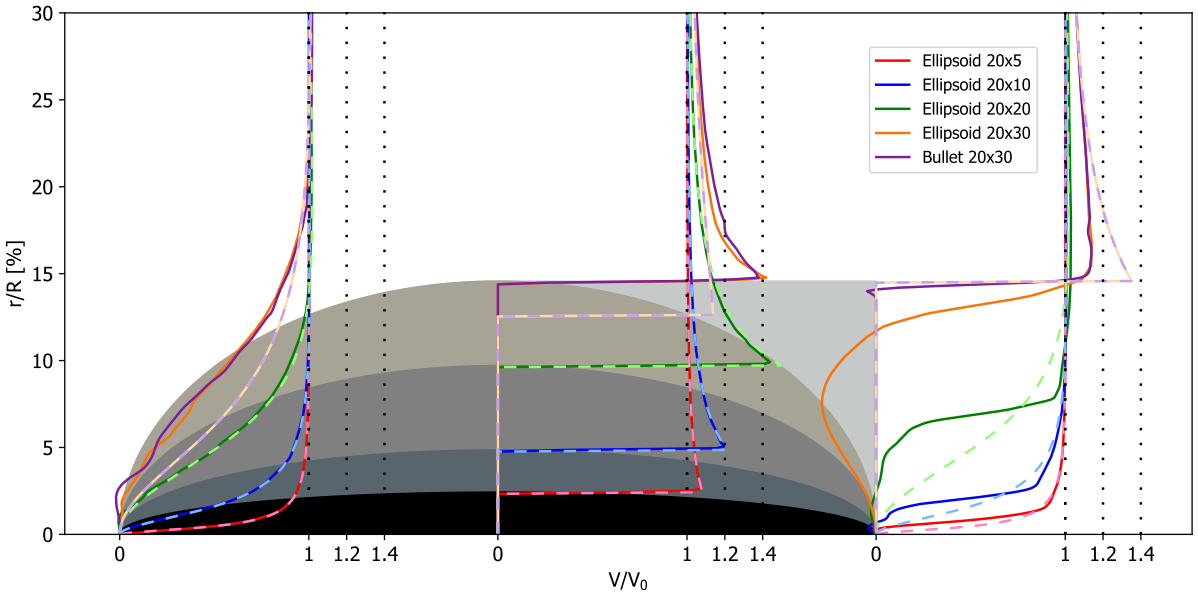

Figure 6. Speedup along the rotor plane for various nacelle heights. The three rotor planes considered, from left to right, are: upwind, middle, and downwind. Solid lines: CFD results. Dashed lines: EM results. Geometry format: (length x height)[m]. Note: 20 x 30-m EM is narrower than the real nacelles at the midplane.

Results are tabulated in Table 3 and plotted in Figure 6 and Figure 5. As expected, increasing nacelle height increases the average speedup along the rotor, leading to increased rotor loads and performance. However, significant increases in rotor performance are only realized in very tall nacelles. In the downwind rotor plane, the 20 x 30-m ellipsoid shows a C_p increase of 0.61% and the 20 x 30-m bullet shows a C_p increase of 0.54%. With the original method, the EM matches CFD results best for high-aspect-ratio nacelles, and their results diverge for lower aspect ratios. The oversize ellipsoid method shows good agreement for the tallest (lowest-aspect-ratio) ellipsoid and bullet, but the original method works better for the spherical nacelle. Hence, the oversize ellipsoid method is considered a candidate option for low-aspect-ratio nacelles or nacelles with different suitable geometries, like the bullet.

3.4. Suite 4: Influence of Reynolds number

Nacelle blockage effects are examined for a variety of Re. Theoretically, boundary layer height (BLH) is dependent upon Re, so boundary layer height, max speedup, and the resulting change in rotor C_p are examined against Re. Two Re's are considered: Re_L is based on nacelle length, and Re_H is based on nacelle height. BLH is defined as the height above the nacelle at which the flow reaches 99% of its maximum velocity. Results are tabulated in Table 4.

Table 4. Flow/BEM results for suite 4 (ellipsoid with varying inflow velocity). Increasing Re has little effect on blockage-induced changes in rotor loads and performance.

U [m/s]	Re_L	Re_H	$\mid \Delta V \mid_{\mathrm{CFD}}$	ΔCP_{CFD}	ΔCT_{CFD}	$\Delta Edge_{\mathrm{CFD}}$	$\Delta Flap_{\mathrm{CFD}}$	$E_{\Delta V}$	E_{CP}
3	3.31e8	1.65e8	2.88%	0.06%	0.03%	0.04%	0.02%	-21.28%	-8.25%
15	1.66e9	8.28e8	2.81%	0.05%	0.03%	0.03%	0.03%	-19.35%	-15.68%
25	2.76e9	1.38e9	2.39%	0.06%	0.03%	-1.95%	0.20%	-5.24%	-15.95%

Generally, there are no significant correlations between Re_L or Re_H and boundary layer height, maximum speedup, or C_p. However, for the ellipsoids, there is a negative correlation

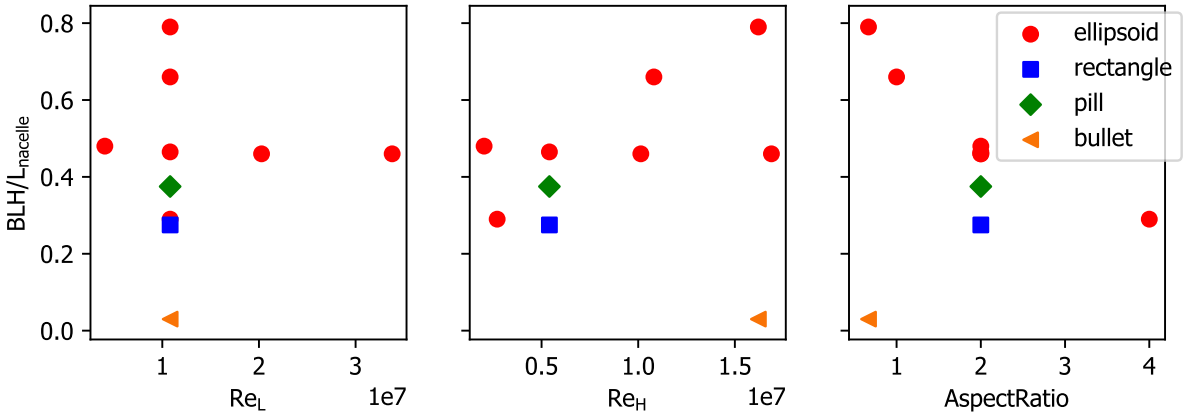

Figure 7. BLH from CFD vs. Re_L, Re_H, and aspect ratio for all nacelles. No correlation is found between BLH and Re, though an inverse relationship is found between BLH and aspect ratio.

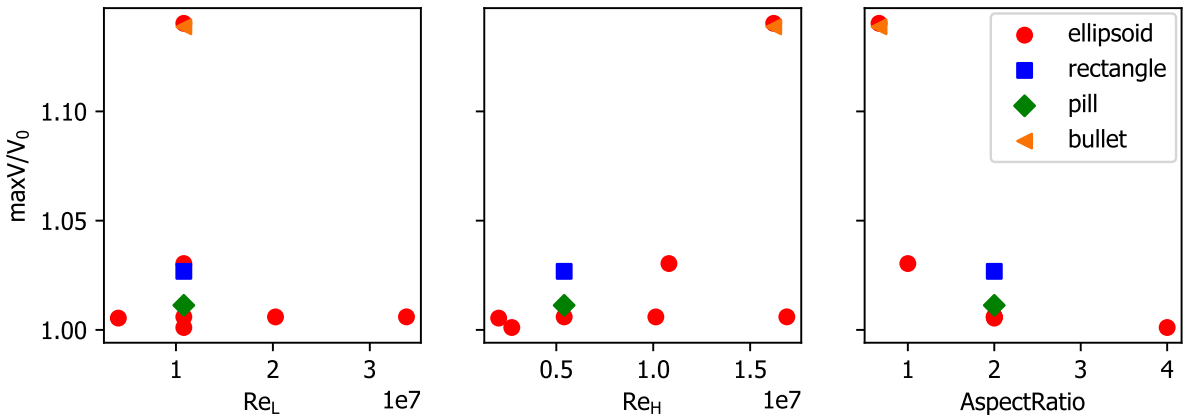

Figure 8. Maximum speedup from CFD vs. Re_L, Re_H, and aspect ratio for all nacelles. No correlation is found between maximum speedup and Re, though an inverse relationship is found between maximum speedup and aspect ratio.

between aspect ratio and all three parameters. This is expected, as fatter nacelles should have thicker boundary layers and larger speedups, with greater effects on power. Finally, modifying Re alone (by varying the freestream velocity) has little bearing on blockage effects. Based on these results, there seems to be little reason for the EM to include specific Re considerations.

3.5. Suite 5: Influence of inflow turbulence intensity and body representation

Nacelle blockage effects are examined for a variety of TIs. Based on results (not shown), varying TI does not significantly affect nacelle blockage. The highest TI considered yielded an increase in C_P of merely 0.01% for the 20 x 10-m ellipsoid nacelle. Geometry-resolved models are compared to body-force models. Their flow results do not match well, with body-force models yielding blockage effects on an order of magnitude larger. This is likely because of the body-force model design to model far-field wake, not nacelle blockage speedup and near-field wake, as seen in Figure 10.

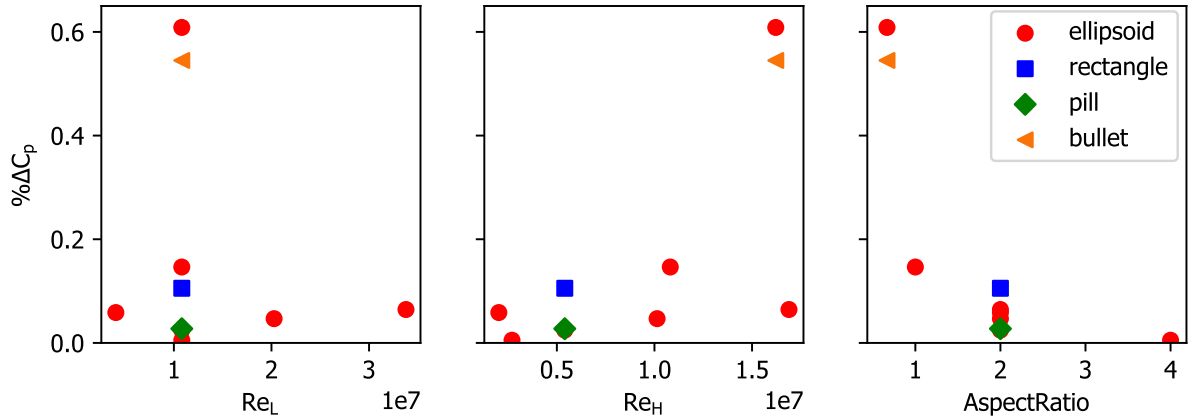

Figure 9. Rotor C_p in CFD flow field vs. Re_L, Re_H, and aspect ratio for all nacelles. No correlation is found between C_p and Re, though an inverse relationship is found between C_p and aspect ratio.

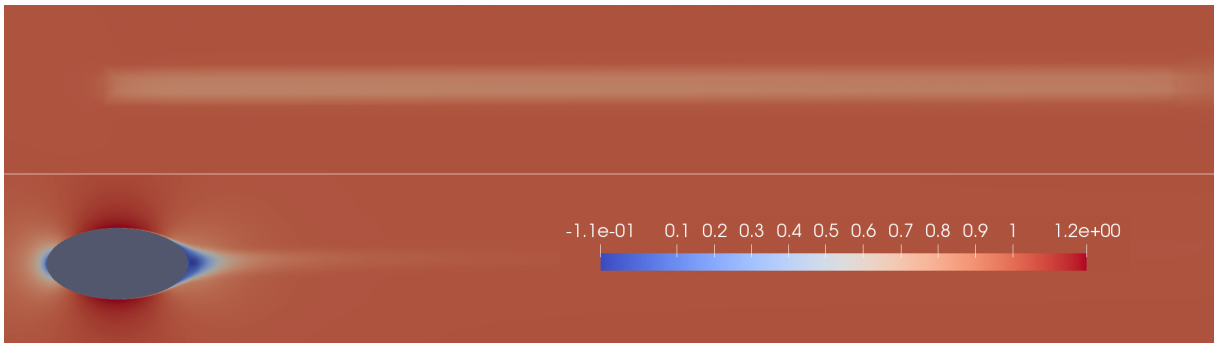

Figure 10. Normalized flow field from body-force (top) and geometry-resolved (bottom) models.

4. Conclusions

CFD models were used to examine nacelle blockage effects on rotor loads and performance. They were found to be insignificant (<0.5%) for all except low-aspect-ratio nacelles. For all cases studied, nacelle blockage was seen to *increase* rotor loads and performance.

The potential-flow EM developed here has negligible (sub-millisecond) computational cost, facilitating its integration into a code such as OpenFAST. For comparison, Fluent's execution time was on the order of 10 minutes. The EM was validated against CFD, yielding fairly similar BEM results, with both models yielding ΔC_p within 0.7% for all runs. For cases with the most significant blockage effects (20 x 30-m ellipsoid and bullet), the relative error in ΔC_p between the two models was within 1% and 11%, respectively. The EM struggled to match the blockage effects of some non-ellipsoid nacelles (rectangular prism and pill). A wake model was considered for integration into the EM but rejected because the EM consistently yielded lower changes in rotor performance than CFD, and the wake model would increase this disparity. Finally, the original EM method was not applicable for nacelles with an aspect ratio of >1, and the oversize ellipsoid method modification was used. The EM should be expanded to handle different and more complex geometries. This EM may be implemented in the OpenFAST code to facilitate downwind turbine design in the future.

Finally, geometry-resolved and body-force models were compared, and body-force models were found to need refinement to adequately model nacelle blockage.

There are several relevant ways to expand this study. Factors that should be considered in further nacelle blockage modeling include dynamic turbulence effects (that drive turbine loading), different and more detailed nacelle geometries, considerations regarding the number of blades, and airfoils optimized for nacelle blockage. The development of body-force models for nacelle blockage and the development of EMs that match CFD results for a wide array of nacelle geometries (particularly low-aspect-ratio geometries) should be considered.

Acknowledgements
The authors would like to thank Dr. Shreyas Ananthan for his valuable input in implementing the turbulence injection algorithm and for his overall guidance on CFD simulations using the ExaWind framework. We also thank Dr. Paula Doubrawa for her guidance in generation of the inflow turbulence using the Mann model and Dr. Tony Martinez for his guidance in implementing the body-force runs.

This work was authored by the National Renewable Energy Laboratory (NREL), operated by Alliance for Sustainable Energy, LLC, for the U.S. Department of Energy (DOE). Funding was provided by DOE's Office of Energy Efficiency and Renewable Energy Wind Energy Technologies Office. The views expressed in the article do not necessarily represent the views of DOE or the U.S. Government. The U.S. Government retains and the publisher, by accepting the article for publication, acknowledges that the U.S. Government retains a non-exclusive, paid-up, irrevocable, worldwide license to publish or reproduce the published form of this work, or allow others to do so, for U.S. Government purposes.

References

[1] OpenFAST. Open-source wind turbine simulation tool, available at `http://github.com/OpenFAST/OpenFAST/`.
[2] Ameur, K., Masson, C. & Eecen, P. J. 2D and 3D numerical simulation of the wind-rotor/nacelle interaction in an atmospheric boundary layer. *Journal of Wind Engineering and Industrial Aerodynamics* **99**, 833–844 (2011).
[3] Wang, Z., Tian, W. & Hu, H. A Comparative study on the aeromechanic performances of upwind and downwind horizontal-axis wind turbines. *Energy Conversion and Management* **163**, 100–110 (2018).
[4] Frau, E., Kress, C., Chokani, N. & Abhari, R. S. Comparison of performance and unsteady loads of multimegawatt downwind and upwind turbines. *Journal of Solar Energy Engineering, Transactions of the ASME* **137**, 1–8 (2015).
[5] Bortolotti, P., Kapila, A. & Bottasso, C. L. Comparison between upwind and downwind designs of a 10-MW wind turbine rotor. *Wind Energy Science* **4**, 115–125 (2019).
[6] Santoni, C., Carrasquillo, K., Arenas-Navarro, I. & Leonardi, S. Effect of tower and nacelle on the flow past a wind turbine **20**, 1927–1939 (2017).
[7] Kress, C. *et al.* Impact of flow inclination on downwind turbine loads and power. *Journal of Physics: Conference Series* **753**, 022011 (2016).
[8] Sprague, M. A., Ananthan, S., Vijayakumar, G. & Robinson, M. No Title. In *"ExaWind: A multifidelity modeling and simulation environment for wind energy", NAWEA/WindTech 2019 Conference* (Amherst, MA, 2019).
[9] Churchfield, M. J. *et al.* A large-eddy simulation of wind-plant aerodynamics. In *Proceedings of the 50th AIAA Aerospace Sciences Meeting including the New Horizons Forum and Aerospace Exposition* (2012).
[10] Martínez-Tossas, L. A. *Large Eddy Simulations and Theoretical Analysis of Wind Turbine Aerodynamics Using an Actuator Line Model.* Ph.D. thesis, Johns Hopkins University, Baltimore, MD USA (2017).
[11] Mann, J. Wind field simulation. *Probabilistic Engineering Mechanics* **13**, 269 – 282 (1998). URL `http://www.sciencedirect.com/science/article/pii/S0266892097000362`.
[12] Troldborg, N., Gaunaa, M. & Guntur, S. Modelling the influence of yaw using a simple vortex rotor model. In *EWEC, Copenhagen*, 1–5 (2012).
[13] Lamb, H. *Hydrodynamics* (Cambridge University Press, Fourth Edition, 1916). Chapter 105 pp 140-146.
[14] Branlard, E. *Wind Turbine Aerodynamics and Vorticity-Based Methods: Fundamentals and Recent Applications* (Springer International Publishing, 2017). Chapter 10 pp 181-211.